Journal of Solid State Chemistry 182 (2009) 1524–1528

Contents lists available at ScienceDirect

Journal of Solid State Chemistry

journal homepage: www.elsevier.com/locate/jssc

Structural and electrical properties evolution in $Ba_{1-x}Sr_xRuO_3$ synthesized under high pressure

Jinggeng Zhao [a,b], Liuxiang Yang [a], Yong Yu [a], Fengying Li [a], Richeng Yu [a], Changqing Jin [a,*]

[a] Beijing National Laboratory for Condensed Matter Physics, Institute of Physics, Chinese Academy of Sciences, Beijing 100190, PR China
[b] Natural Science Research Center, Academy of Fundamental and Interdisciplinary Sciences, Harbin Institute of Technology, Harbin 150080, PR China

ARTICLE INFO

Article history:
Received 24 January 2009
Received in revised form
9 March 2009
Accepted 14 March 2009
Available online 21 March 2009

Keywords:
High-pressure synthesis
6H-perovskite
A-site solid solutions
Electrical conductivity

ABSTRACT

The 6H and 6M $Ba_{1-x}Sr_xRuO_3$ at $x \leqslant 0.6$ with the normal and distorted hexagonal $BaTiO_3$ structures were synthesized by using high-pressure and high-temperature method. It is found that the unit cell volume deviates from Vegard's law between 0.3 and 0.4 for the solid solutions due to the increasing distortion degree of crystal structure. With the increasing x, the electrical resistivity at the same temperature is increasing. With the substitution of Sr for Ba ion, the 6H $BaRuO_3$ transforms to a Fermi-liquid metal at $x = 0.25$ from the primal non-Fermi-liquid metal, and then becomes a semiconductor at low temperature when x is larger than 0.4.

1. Introduction

The oxide ruthenates have received growing attention for their unique physical properties. For example, Sr_2RuO_4, with the K_2NiF_4-type structure, is a superconductor of unconventional *p*-wave paring mechanism [1]. The alkaline-earth ruthenate $ARuO_3$ (A = Ca, Sr, and Ba) is an important system of oxide ruthenates [2]. $SrRuO_3$ and $CaRuO_3$ adopt the orthorhombic perovskite structure with the space group *Pnma* [3,4]. There are three types of hexagonal perovskite-type $BaRuO_3$ reported, namely 9R, 4H, and 6H [5–7], where the number is the amount of BaO_3 layers in a unit cell, and the R and H denote the rhombohedral (space group: *R*-3*m*) and hexagonal (space group: $P6_3/mmc$) structures, respectively.

With the decreasing temperature, the 9R $BaRuO_3$ transforms to insulator-like from metallic behavior at about 110 K due to the pseudogap open [8,9]. It is of short-range antiferromagnetic order at high temperature, with the Néel point about 440 K [9,10]. The 4H $BaRuO_3$ is paramagnetic down to liquid helium temperature [8]. It is a normal Fermi-liquid metal. Recently, we have obtained the pure 6H $BaRuO_3$ at 5 GPa and 1000 °C [11], and found that it is an abnormal paramagnetic metal deviated from the Fermi-liquid behavior [11].

The chemical substitution of M cation for 1/3 Ru cation at ambient pressure can make the 9R $BaRuO_3$ transform to the $Ba_3MRu_2O_9$ compounds, where M = alkali metals, alkaline-earth elements, 3*d* transition metals, and lanthanide elements. They adopt the normal or distorted hexagonal $BaTiO_3$ structures [12,13]. Longo et al. synthesized the $Ba_{1-x}Sr_xRuO_3$ solutions using high-pressure sintering at 1000 °C up to 9 GPa and indicated that both high pressure and chemical substitution can make $BaRuO_3$ transform to perovskite across the 4H and 6H forms from the primal 9R form [7]. However, the structural and physical properties of this series and the correlations between the RuO_6 polyhedron connections with their physics have not been available so far due to the difficulty to prepare single-phase samples.

In this paper, we successfully obtained the 6H $Ba_{1-x}Sr_xRuO_3$ series by using the high-pressure and high-temperature synthesis method and found that the solutions transform to the distorted hexagonal $BaTiO_3$ structure with the space group $C2/c$ at $x \geqslant 0.4$, which is different from the results in [7]. The structure of our 6M form is similar with that of the ambient-pressure phase of $SrIrO_3$ [14], so it is denoted to 6M. Fig. 1(a) and (b) show the schematic views of the 6H and 6M $Ba_{1-x}Sr_xRuO_3$, respectively. For the first time the structural detail based on Rietveld refinement, together with the systematic characterization of electrical properties of the 6H and 6M $Ba_{1-x}Sr_xRuO_3$ ($0.0 \leqslant x \leqslant 0.6$) was obtained.

2. Experimental

The ambient phases of $Ba_{1-x}Sr_xRuO_3$ were synthesized by using the method of conventional solid-state chemical reaction. The starting materials were barium and strontium carbonates

* Corresponding author. Fax: +86 10 82640223.
E-mail address: zhaojinggeng@163.com (C.Q. Jin).

0022-4596/$ - see front matter © 2009 Elsevier Inc. All rights reserved.
doi:10.1016/j.jssc.2009.03.007

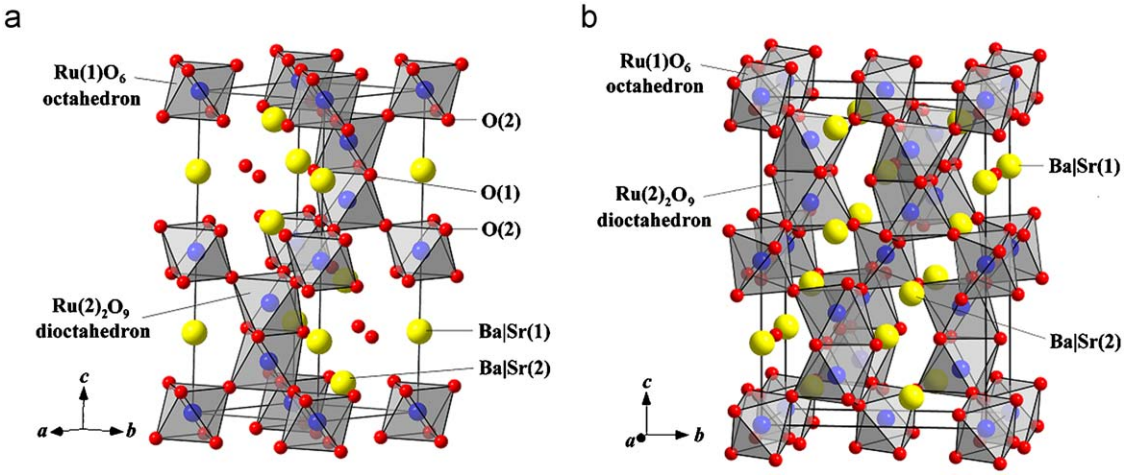

Fig. 1. The schematic views of the crystallographic forms of $Ba_{1-x}Sr_xRuO_3$: (a) 6H form and (b) 6M form. The RuO_6 octahedrons are represented by geometrical coordination (Ru at the center, O at corners). The unit cells are outlined.

(99.9% purity) and ruthenium metal (99.9% purity). Stoichiometric quantities of materials were mixed together, ground about 30 min in an agate mortar, and placed into an Al_2O_3 crucible. Then the powder was calcined for about 12 h at 1000 °C in air. The calcined powder was reground, pressed into a pellet at the pressure of 10 MPa, and sintered at 1100 °C for about 48 h in air with twice intermediate regrinding. The products were polycrystalline powder in black.

A conventional cubic-anvil type high-pressure facility was used to perform the high-pressure and high-temperature experiments. The ambient $Ba_{1-x}Sr_xRuO_3$ were pressed into pellets of 5.0 mm diameter, and then wrapped with gold foil to avoid contamination. The pellets were put into an h-BN sleeve which was in turn inserted into a graphite tube heater. Pyrophyllite was used as the pressure-transmitting medium. The treating process was carried out at 1.5–5.0 GPa and 1000 °C for about 30 min, followed by a quench from high temperature before releasing pressure with the rate about 0.6 GPa/min. The 6H $Ba_{1-x}Sr_xRuO_3$ ($0.0 \leqslant x \leqslant 0.3$) are obtained at 5.0 GPa, and the 6M phases are synthesized at 4.5 GPa ($x = 0.4$), 3.5 GPa ($x = 0.5$), and 1.5 GPa ($x = 0.6$).

The structures of our samples were checked by the powder X-ray diffraction (XRD) with Cu$K\alpha$ radiation at room temperature, using a Rigaku diffractometer (MXP-AHP18). The experimental data for the $x = 0.0$, 0.1, 0.2, 0.3, 0.6 samples were collected in 2θ-steps of 0.02° and 3 s counting time in the range of 10°–120° and analyzed with Rietveld method by using the FullProf program [15]. The measurements of temperature dependences of electrical resistivity were performed by using the standard four-probe method with Ag paste contacts in the temperature range of 3–300 K on an Oxford Maglab.

3. Results and discussion

3.1. Crystal structure

Fig. 2(a) shows the observed and fitted XRD patterns of the 6H $Ba_{0.8}Sr_{0.2}RuO_3$. The XRD data are fitted with the $P6_3/mmc$ space group and analyzed with the Rietveld method. Table 1 lists the lattice parameters, atomic positional parameters, and conventional Rietveld R-factors for the 6H $Ba_{1-x}Sr_xRuO_3$ ($0.0 \leqslant x \leqslant 0.3$). The obtained R_p, R_{wp}, and R_{exp} factors indicate the good

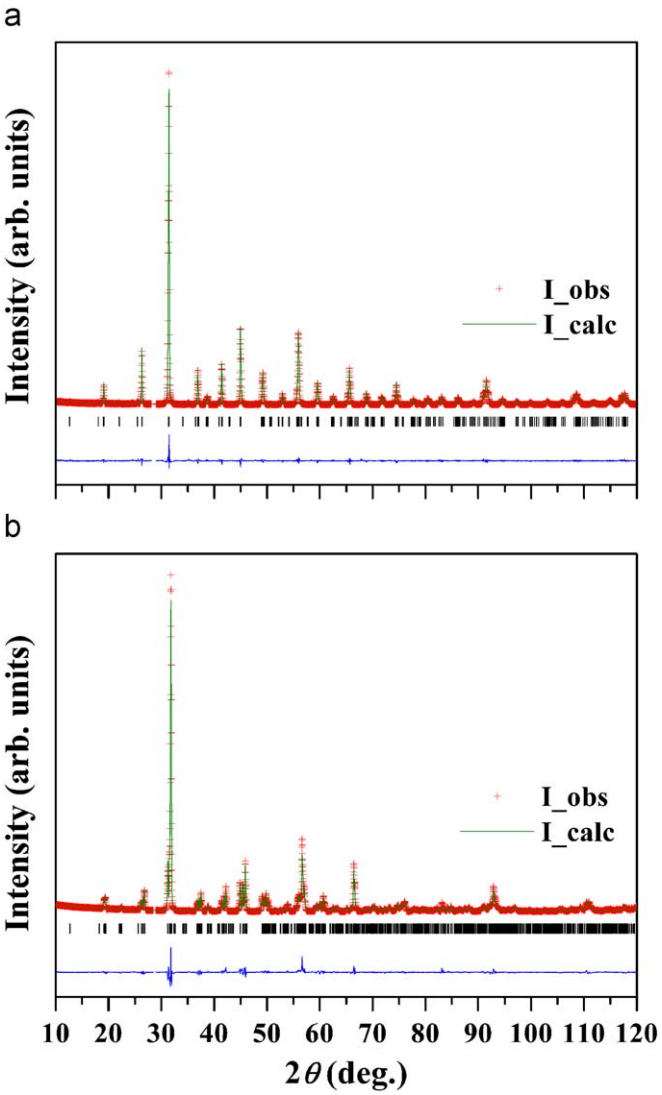

Fig. 2. The experimental (cross) and fitted (solid line) X-ray diffraction patterns for $Ba_{1-x}Sr_xRuO_3$: (a) the 6H $Ba_{0.8}Sr_{0.2}RuO_3$ and (b) the 6M $Ba_{0.4}Sr_{0.6}RuO_3$. The difference plots between observed and calculated patterns are shown at the bottom. The positions of the Bragg reflections are shown by the vertical lines.

Table 1
Lattice parameters, conventional Rietveld *R*-factors, and atomic coordinates for the 6H $Ba_{1-x}Sr_xRuO_3$ ($0.0 \leqslant x \leqslant 0.3$).

	Site	*x* in $Ba_{1-x}Sr_xRuO_3$			
		0.0	0.1	0.2	0.3
a (Å)		5.7127(1)	5.6999(1)	5.6873(1)	5.6749(2)
c (Å)		14.0499(2)	14.0317(2)	14.0121(3)	13.9943(4)
Ba|Sr(1) *B* (Å^2)	2*b*	0.35(3)	0.55(6)	0.41(6)	0.27(9)
Ba|Sr(2) *z*		0.08960(6)	0.08995(6)	0.09022(6)	0.09086(8)
Ba|Sr(2) *B* (Å^2)	4*f*	0.22(2)	0.61(3)	0.29(2)	0.26(3)
Ru(1) *B* (Å^2)	2*a*	0.62(4)	0.53(7)	0.75(7)	0.37(6)
Ru(2) *z*		0.65869(6)	0.65910(7)	0.65922(6)	0.65930(7)
Ru(2) *B* (Å^2)	4*f*	0.40(3)	0.68(3)	0.51(3)	0.62(4)
O(1) *x*		0.517(1)	0.511(1)	0.510(1)	0.510(1)
O(1) *B* (Å^2)	6*h*	1.7(2)	1.8(2)	1.5(2)	1.4(2)
O(2) *x*		0.836(1)	0.836(1)	0.834(1)	0.836(1)
O(2) *z*		0.078(1)	0.082(1)	0.082(1)	0.084(1)
O(2) *B* (Å^2)	12*k*	0.4(1)	0.9(1)	1.9(1)	1.1(1)
R_p (%)		6.12	5.34	5.15	6.14
R_{wp} (%)		8.47	7.79	7.59	9.01
R_{exp} (%)		7.54	7.56	7.24	7.36

Table 2
Selected interatomic distances (Å) and angles (deg) for the 6H $Ba_{1-x}Sr_xRuO_3$ ($0.0 \leqslant x \leqslant 0.3$).

	x in $Ba_{1-x}Sr_xRuO_3$			
	0.0	0.1	0.2	0.3
Ba|Sr(1)–O(1) × 6	2.861(4)	2.852(4)	2.845(4)	2.839(4)
Ba|Sr(1)–O(2) × 6	2.911(13)	2.860(12)	2.866(12)	2.828(12)
Ba|Sr(2)–O(1) × 3	2.895(4)	2.850(3)	2.836(3)	2.824(3)
Ba|Sr(2)–O(2) × 6	2.861(4)	2.852(4)	2.846(4)	2.839(4)
Ba|Sr(2)–O(2) × 3	2.890(13)	2.935(12)	2.922(12)	2.959(12)
Ru(2)–O(1) × 3	1.959(5)	1.997(5)	2.000(5)	1.996(5)
Ru(2)–O(2) × 3	2.023(11)	1.991(9)	1.972(9)	1.970(9)
Ru(2)–O (average)	1.991(8)	1.994(7)	1.986(7)	1.983(7)
Ru(2)–Ru(2)	2.566(1)	2.551(1)	2.544(1)	2.539(1)
Ru(1)–Ru(2)	3.9811(6)	3.9766(6)	3.9698(5)	3.9629(6)
Ru(1)–O(2) × 6	1.958(10)	1.986(10)	1.999(10)	1.995(10)
O(1)–Ru(2)–O(1) × 3	81.8(1)	83.6(1)	83.9(1)	83.9(1)
O(1)–Ru(2)–O(2) × 6	93.1(3)	91.4(2)	91.5(2)	90.8(2)
O(2)–Ru(2)–O(2) × 3	91.7(3)	93.3(2)	92.8(3)	94.1(2)
O(1)–Ru(2)–O(2) × 3	173.2(3)	173.2(2)	173.8(2)	172.8(2)
Ru(2)–O(1)–Ru(2)	81.8(1)	79.4(1)	79.0(1)	79.0(1)
O(2)–Ru(1)–O(2) × 6	88.3(3)	89.8(3)	89.8(3)	88.8(3)
O(2)–Ru(1)–O(2) × 6	91.7(3)	90.2(3)	90.2(3)	91.2(3)
O(2)–Ru(1)–O(2) × 3	180.0(5)	180.0(1)	180.0(1)	180.0(1)
Ru (2)–O(2)–Ru (1)	180.0(6)	177.5(3)	178.2(3)	176.2(3)

Table 3
Atomic coordinates for the 6M $Ba_{0.4}Sr_{0.6}RuO_3$.

Atom	Site	*x*	*y*	*z*	*B* (Å^2)
Ba|Sr(1)	4*e*	0	0.0031(4)	1/4	0.8(1)
Ba|Sr(2)	8*f*	0.0062(3)	0.6668(3)	0.0927(1)	0.61(5)
Ru(1)	4*a*	0	0	0	0.48(9)
Ru(2)	8*f*	0.9899(3)	0.6676(4)	0.8403(1)	0.63(4)
O(1)	4*e*	0	0.526(3)	1/4	2.4(5)
O(2)	8*f*	0.254(2)	0.256(1)	0.257(1)	1.8(3)
O(3)	8*f*	0.768(3)	0.414(2)	0.072(1)	1.3(3)
O(4)	8*f*	0.967(2)	0.153(2)	0.413(1)	1.6(3)
O(5)	8*f*	0.278(2)	0.424(2)	0.092(1)	1.1(3)

Table 4
Selected bond distances (Å) for the 6M $Ba_{0.4}Sr_{0.6}RuO_3$.

Bond	Distance (Å)
Ba|Sr(1)–O(1) × 2	2.882(2)
Ba|Sr(1)–O(2) × 2	2.905(11)
Ba|Sr(1)–O(2) × 2	2.835(11)
Ba|Sr(1)–O(3) × 2	3.139(16)
Ba|Sr(1)–O(4) × 2	2.782(16)
Ba|Sr(1)–O(5) × 2	2.692(14)
Ba|Sr(1)–O(average)	2.873(14)
Ba|Sr(2)–O(1)	2.655(16)
Ba|Sr(2)–O(2)	2.682(13)
Ba|Sr(2)–O(2)	2.932(14)
Ba|Sr(2)–O(3)	2.837(16)
Ba|Sr(2)–O(3)	2.898(19)
Ba|Sr(2)–O(3)	2.871(19)
Ba|Sr(2)–O(4)	3.011(26)
Ba|Sr(2)–O(4)	3.033(12)
Ba|Sr(2)–O(4)	3.141(16)
Ba|Sr(2)–O(5)	2.871(19)
Ba|Sr(2)–O(5)	2.873(18)
Ba|Sr(2)–O(5)	3.209(14)
Ba|Sr(2)–O(average)	2.918(17)
Ru(1)–O(3) × 2	2.023(17)
Ru(1)–O(4) × 2	1.972(18)
Ru(1)–O(5) × 2	2.004(14)
Ru(1)–O(average)	2.000(16)
Ru(2)–O(1)	2.319(25)
Ru(2)–O(2)	2.095(13)
Ru(2)–O(2)	2.097(13)
Ru(2)–O(3)	2.023(17)
Ru(2)–O(4)	2.070(19)
Ru(2)–O(5)	2.052(15)
Ru(2)–O(average)	2.109(17)
Ru(2)–Ru(2)	2.596(2)

consistence of the refined results. Table 2 lists the main interatomic distances and bond angles. The average Ru–O distance is decreasing with the increasing *x* except the value of $Ba_{0.9}Sr_{0.1}RuO_3$. The Ru–Ru distance for the two Ru cations connected directly in the Ru_2O_9 dioctahedron is decreasing with the increasing *x*. The O(2)–Ru–O(2) angles are nearly equal to 90° or 180°, which indicates that the RuO_6 octahedrons are close to ideal ones. The O(1)–Ru–O(1), O(2)–Ru–O(2), and O(1)–Ru–O(2) angles deviate from 90° or 180°, indicating that the distortion degree of the Ru_2O_9 dioctahedrons is larger than that of the RuO_6 octahedrons for all the solid solutions. The Ru(2)–O(2)–Ru(1) angle is basically decreasing with the increasing *x*, which indicates that the distortion degree of crystal structure is increasing.

Fig. 2(b) shows the observed and fitted XRD patterns of the 6M $Ba_{0.4}Sr_{0.6}RuO_3$. The XRD data are fitted with the *C*2/*c* space group and analyzed with the Rietveld method. The obtained R_p, R_{wp}, and R_{exp} factors are 7.52%, 9.77%, and 2.58%, respectively, which indicate the good consistence of the refined results. The lattice parameters are refined to be $a = 5.6294(1)$ Å, $b = 9.7387(2)$ Å, $c = 13.9408(3)$ Å, and $\beta = 91.437(1)°$. Table 3 lists the positional parameters. Table 4 and 5 list the main interatomic distances and bond angles, respectively. The distortion in the BaO_{12} icosahedrons is large, since the Ba–O distances are in the range of 2.692–3.139 and 2.655–3.209 Å for the Ba(1)O_{12} and Ba(2)O_{12} icosahedrons, respectively. The Ru(2)–Ru(2) distance is 2.596(1) Å for the two neighboring Ru cations in the Ru(2)$_2O_9$ dioctahedron. The Ru–Ru distances in the dioctahedron are shorter than the separation in ruthenium metal (2.65 Å). So there is strong repulsion between the adjacent Ru cations in the 6M $Ba_{0.4}Sr_{0.6}RuO_3$, which can induce that $Ba_{1-x}Sr_xRuO_3$ have a large bulk modulus. All the O–Ru–O angles deviate from 90° or 180°, which indicates that both the Ru(2)$_2O_9$ dioctahedron and the Ru(1)O_6

Table 5
Selected bond angles (deg) for the 6M $Ba_{0.4}Sr_{0.6}RuO_3$.

Bond	Angle (deg)
O(1)–Ru(2)–O(2)	87.3(3)
O(1)–Ru(2)–O(2)	87.3(3)
O(1)–Ru(2)–O(3)	89.4(5)
O(1)–Ru(2)–O(4)	175.8(5)
O(1)–Ru(2)–O(5)	85.7(5)
O(2)–Ru(2)–O(2)	88.3(5)
O(2)–Ru(2)–O(3)	90.2(6)
O(2)–Ru(2)–O(3)	176.5(6)
O(2)–Ru(2)–O(4)	88.5(5)
O(2)–Ru(2)–O(4)	91.8(5)
O(2)–Ru(2)–O(5)	88.8(5)
O(2)–Ru(2)–O(5)	172.6(5)
O(3)–Ru(2)–O(4)	94.7(6)
O(3)–Ru(2)–O(5)	92.3(6)
O(4)–Ru(2)–O(5)	94.9(6)
O(3)–Ru(1)–O(3)	180.0(7)
O(3)–Ru(1)–O(4)	86.6(6)
O(3)–Ru(1)–O(4)	93.4(6)
O(3)–Ru(1)–O(5)	89.6(6)
O(3)–Ru(1)–O(5)	90.4(6)
O(4)–Ru(1)–O(4)	180.0(1)
O(4)–Ru(1)–O(5)	85.8(6)
O(4)–Ru(1)–O(5)	94.2(6)
O(5)–Ru(1)–O(5)	180.0(1)
Ru(1)–O(3)–Ru(2)	172.2(9)
Ru(1)–O(4)–Ru(2)	167.2(9)
Ru(1)–O(5)–Ru(2)	167.1(7)
Ru(2)–O(1)–Ru(2)	68.1(1)
Ru(2)–O(2)–Ru(2)	76.5(5)

octahedron are distorted from the idea ones. The average Ru(2)–Ru(2) distance is larger than that in the 6H forms, due to the larger distortion of crystal lattice.

The lattice parameters are calculated from Rietveld and Le Bail refinements for the $x = 0.0, 0.1, 0.2, 0.3, 0.6$ samples and $x = 0.4$, 0.5 samples, respectively. Fig. 3(a) shows the relationships of pseudocubic lattice parameter a_N, b_N, and c_N, and β versus x ($0.0 \leqslant x \leqslant 0.6$), where $a_N = a/\sqrt{2}$, $b_N = b/\sqrt{6}$, and $c_N = c \sin \beta/(2\sqrt{3})$. Using these equations, the hexagonal unit cell can be normalized to an assumed pseudocubic perovskite form, in which the hexagonal structure contains a sequence of six close-packed layers, with each layer consisting of the same ions of the (111) plane in the cubic structure [12]. With the increasing x, a_N, b_N, and c_N are decreasing, due to the smaller ionic radius of Sr cation comparing with Ba cation [16]. The substitution of Sr for Ba cation results in the similar compressing effect on the crystal lattice with high pressure [7]. The inset in Fig. 3(a) shows the x dependence of normalized lattice parameters at $0.0 \leqslant x \leqslant 0.3$. The values of a- and c-axis are both decreasing with the increasing x, and the change of c with x is smaller than that of a. The c_N is larger than a_N for all the solid solutions of $Ba_{1-x}Sr_xRuO_3$ ($0.0 \leqslant x \leqslant 0.6$). Fig. 3(b) shows the relationship of the ratio of c_N to a_N (c_N/a_N) versus x. The value of c_N/a_N is increasing with the increasing x, which indicates that it is easier to compress the ab-plane, comparing with the c-axis, because of the strong repulsion between the neighbouring Ru cations along the c-axis in the Ru_2O_9 dioctahedron. For the 6M forms, with the increasing x, a_N, b_N, and c_N are decreasing, and β is increasing, which indicates the increasing distortion degree of crystal structure with x.

Fig. 3(b) shows the relationship of the volume of one chemical formula unit (V_N) versus the Sr content x in the 6H and 6M $Ba_{1-x}Sr_xRuO_3$ ($0.0 \leqslant x \leqslant 0.6$), where V_N is equal to $V/6$ and $V/12$ for the 6H and 6M forms, respectively. The relationship of V_N versus x should be linear because of the disordered arrangement of Ba and Sr cations. However, there is an obvious variation between 0.3 and 0.4. The value of $\partial(V_N)/\partial x$ is $-3.80(1)$ Å^3 for $x \leqslant 0.3$ and $-5.8(2)$ Å^3 for $x \geqslant 0.4$. So the x dependence of V_N deviates from the Vegard's law, due to the crystal structure transition at $x = 0.4$, which is like that in $Sr_{1-x}Ca_xCrO_3$ ($0.0 \leqslant x \leqslant 1.0$) solutions in which $SrCrO_3$ transforms to tetragonal structure at $x = 0.4$ from the primal cubic structure [17].

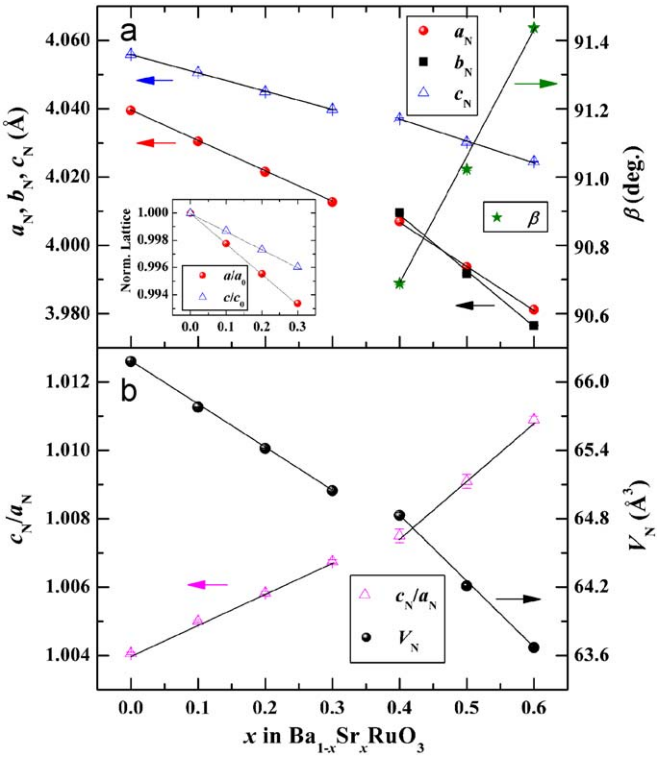

Fig. 3. The relationship of (a) a_N, b_N, c_N and β, and (b) c_N/a_N and V_N versus x ($0.0 \leqslant x \leqslant 0.6$), where $a_N = a/\sqrt{2}$, $b_N = b/\sqrt{6}$, and $c_N = c \sin \beta/(2\sqrt{3})$, and $V_N = V/6$ ($x \leqslant 0.3$) and $V/12$ ($x \geqslant 0.4$). The lines are the guides for the eyes. The inset in Fig. 3(a) shows the relationships of normalized lattice parameters versus x ($0.0 \leqslant x \leqslant 0.3$).

3.2. Electrical properties

The temperature dependences of electrical resistivity in the range of 3–300 K of the 6H and 6M $Ba_{1-x}Sr_xRuO_3$ ($0.0 \leqslant x \leqslant 0.6$) are shown in Fig. 4. The inset shows the x dependences of electrical resistivity at 3, 150 and 300 K. The electrical resistivity at the same temperature is increasing with the increasing x. The change of electrical resistivity is mainly due to the distortion of crystal structure induced by Sr doping. The 6H $Ba_{1-x}Sr_xRuO_3$ ($0.0 \leqslant x \leqslant 0.3$) maintains the metallic behavior down to the lowest temperature in our experiments, which is different from the semiconducting properties of these compounds with Ru-site substitution [18–20]. Among the three hexagonal $BaRuO_3$, the 9R form is metallic at higher temperature, and then transforms to a insulator at about 110 K [8,9]. Both the 4H and 6H forms are metallic down to liquid helium temperature [8,11], but they are not Fermi-liquid metals. Fig. 5(a) shows the x dependence of the index n in the equation $\rho = \rho_0 + AT^n$ calculated from fitting the ρ–T curves at low temperature. For the 6H $BaRuO_3$, n is equal to 3/2 [11]. With Sr doping, n is equal to about 5/3 at $x = 0.05$–0.2 and then reaches about 2 at $x \geqslant 0.25$, which indicates that there exists the Fermi-liquid behavior in these samples.

When x is larger than 0.3, the samples transform to insulators at low temperature from metals at higher temperature. The

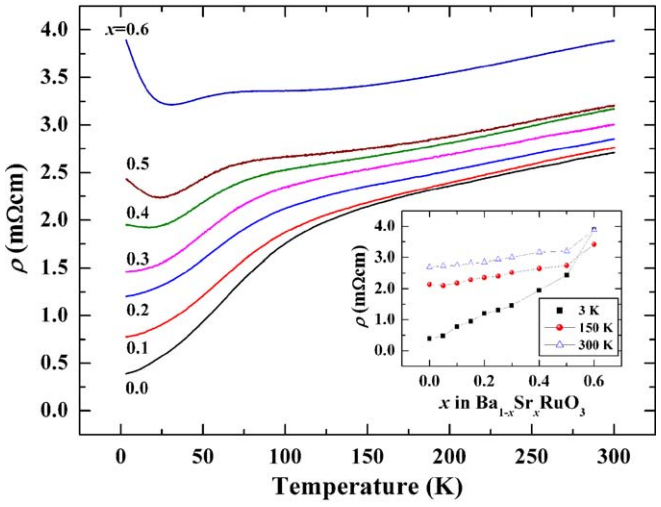

Fig. 4. Temperature dependences of electrical resistivity of the 6H and 6M $Ba_{1-x}Sr_xRuO_3$ ($0.0 \leqslant x \leqslant 0.6$). The inset shows the relationships of resistivity versus x at 3, 150 and 300 K.

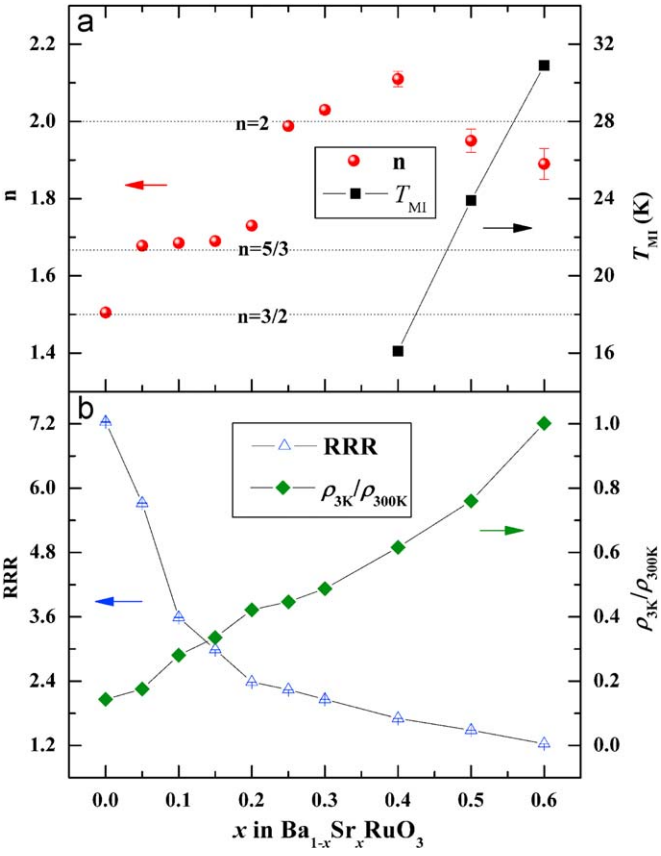

Fig. 5. The relationships of (a) n and T_{MI}, and (b) RRR and ρ_{3K}/ρ_{300K} versus x ($0.0 \leqslant x \leqslant 0.6$), where n is the index in the equation $\rho = \rho_0 + AT^n$, and $RRR = \rho_{300K}/\rho_0$.

metal–insulator transition (MIT) temperature T_{MI} is increasing with the increasing x, as shown in Fig. 5(a), which is attributed to the increasing distortion degree of crystal lattice. The $\rho-T$ curves in the metallic region near T_{MI} can be fitted using the equation $\rho = \rho_0 + AT^n$, where n is close to 2, with the results shown in Fig. 5(a).

The relationship of residual resistivity ratio ($RRR = \rho_{300K}/\rho_0$) versus x for the 6H and 6M $Ba_{1-x}Sr_xRuO_3$ ($0.0 \leqslant x \leqslant 0.6$) is shown in Fig. 5(b). With the increasing x, RRR is decreasing, which indicates that the metallicity becomes worse with Sr doping, due to the increasing distortion degree of crystal structure. Fig. 5(b) also shows the relationship of ρ_{3K}/ρ_{300K} versus x. According to the similar judgment in Ref. [21] , the ratio of resistivity at 3 K to that at 300 K can reflect the electrical property of compounds: $\rho_{3K}/\rho_{300K} < 1$ is corresponding to a metal, and $\rho_{3K}/\rho_{300K} > 1$ is corresponding to a semiconductor. So the 6M $Ba_{1-x}Sr_xRuO_3$ ($0.4 \leqslant x \leqslant 0.6$) can also be approximately viewed as metals, since their ρ_{3K}/ρ_{300K} are close to 1.

4. Conclusion

In conclusion, the 6H and 6M $Ba_{1-x}Sr_xRuO_3$ ($0.0 \leqslant x \leqslant 0.6$) were synthesized by using the high-pressure technique, and the XRD pattern and electrical resistivity were obtained. Structural data indicated that they crystallize into the normal or distorted hexagonal $BaTiO_3$ structure, with the disordered arrangement of Ba and Sr cations. The measurements of electrical properties showed that the substitution of Sr for Ba cation results in the Fermi-liquid behavior from the primal non-Fermi-liquid one for the 6H form and metal–insulator transition for the 6M form.

Acknowledgments

We thank Prof. C. Dong and H. Chen of Institute of Physics, Chinese Academy of Sciences for their help in XRD measurement and analysis, and the support from NSF and Ministry of Science and Technology of China through the research projects.

References

[1] Y. Maeno, H. Hashimoto, K. Yoshida, S. Nishizaki, T. Fujita, J.G. Bednorz, F. Lichtenberg, Nature 372 (1994) 532–534.
[2] M. Shepard, S. McCall, G. Cao, J.E. Crow, J. Appl. Phys. 81 (1997) 4978–4980.
[3] A. Callaghan, C.W. Moeller, R. Ward, Inorg. Chem. 5 (1966) 1572–1576.
[4] J.M. Longo, P.M. Raccah, J.B. Goodenough, J. Appl. Phys. 39 (1968) 1327–1328.
[5] P.C. Donohue, L. Katz, R. Ward, Inorg. Chem. 5 (1966) 335–338.
[6] P.C. Donohue, L. Katz, R. Ward, Inorg. Chem. 4 (1965) 306–310.
[7] J.M. Longo, J.A. Kafalas, Mater. Res. Bull. 3 (1968) 687–692.
[8] J.T. Rijssenbeek, R. Jin, Y. Zadorozhny, Y. Liu, B. Batlogg, R.J. Cava, Phys. Rev. B 59 (1999) 4561–4564.
[9] Y.S. Lee, J.S. Lee, K.W. Kim, T.W. Noh, J. Yu, E.J. Choi, G. Cao, J.E. Crow, Europhys. Lett. 55 (2001) 280–286.
[10] M. Drillon, L. Padel, J.-C. Bernier, J. Chem. Soc. Faraday Trans. II 75 (1979) 1193–1198.
[11] J.G. Zhao, L.X. Yang, Y. Yu, F.Y. Li, R.C. Yu, Z. Fang, L.C. Chen, C.Q. Jin, J. Solid State Chem. 280 (2007) 2816–2823.
[12] R.D. Burbank, H.T. Evans Jr., Acta Crystallogr. 1 (1948) 330–336.
[13] E. Quarez, M. Huvé, F. Abraham, O. Mentré, Solid State Sci. 5 (2003) 951–963.
[14] J.M. Longo, J.A. Kafalas, R.J. Arnott, J. Solid State Chem. 3 (1971) 174–179.
[15] R.A. Young, The Rietveld Method, IUCr/Oxford University Press, Oxford, 1995.
[16] R.D. Shannon, Acta Crystallogr. A 32 (1976) 751–767.
[17] E. Castillo-Martínez, A. Durán, M.Á. Alario-Franco, J. Solid State Chem. 181 (2008) 895–904.
[18] P. Lightfoot, P.D. Battle, J. Solid State Chem. 89 (1990) 174–783.
[19] J.T. Rijssenbeek, P. Matl, B. Batlogg, N.P. Ong, R.J. Cava, Phys. Rev. B 58 (1998) 10315–10318.
[20] Y. Doi, K. Matsuhira, Y. Hinatsu, J. Solid State Chem. 165 (2002) 317–323.
[21] M. Jansen, B. Klinkert, S. Elschner, Mater. Res. Bull. 25 (1990) 1415–1420.